2016

Geometry-coupled reactive fluid transport at the fracture scale: application to CO2 geologic storage

S. Kim

J.C. Santamarina

GEOFLUIDS

Geofluids (2016) **16**, 329–341 doi: 10.1111/gfl.12152

Geometry-coupled reactive fluid transport at the fracture scale: application to CO_2 geologic storage

S. KIM[1] AND J. C. SANTAMARINA[2]

[1]*Department of Civil and Environmental Engineering, Western New England University, Springfield, MA, USA;*
[2]*Division of Physical Science and Engineering, KAUST, Thuwal, Saudi Arabia*

ABSTRACT

Water acidification follows CO_2 injection and leads to reactive fluid transport through pores and rock fractures, with potential implications to reservoirs and wells in CO_2 geologic storage and enhanced oil recovery. Kinetic rate laws for dissolution reactions in calcite and anorthite are combined with the Navier-Stokes law and advection–diffusion transport to perform geometry-coupled numerical simulations in order to study the evolution of chemical reactions, species concentration, and fracture morphology. Results are summarized as a function of two dimensionless parameters: the Damköhler number *Da* which is the ratio between advection and reaction times, and the transverse Peclet number *Pe* defined as the ratio between the time for diffusion across the fracture and the time for advection along the fracture. Reactant species are readily consumed near the inlet in a carbonate reservoir when the flow velocity is low (low transverse Peclet number and $Da > 10^{-1}$). At high flow velocities, diffusion fails to homogenize the concentration field across the fracture (high transverse Peclet number $Pe > 10^{-1}$). When the reaction rate is low as in anorthite reservoirs ($Da < 10^{-1}$), reactant species are more readily transported toward the outlet. At a given Peclet number, a lower Damköhler number causes the flow channel to experience a more uniform aperture enlargement along the length of the fracture. When the length-to-aperture ratio is sufficiently large, say $l/d > 30$, the system response resembles the solution for 1D reactive fluid transport. A decreased length-to-aperture ratio slows the diffusive transport of reactant species to the mineral fracture surface, and analyses of fracture networks must take into consideration both the length and slenderness of individual fractures in addition to *Pe* and *Da* numbers.

Key words: CO_2 geologic storage, mineral dissolution, Navier-Stokes law, reactive fluid transport, rock fracture

Received 7 November 2014; accepted 13 August 2015

Corresponding author: Seunghee Kim, Department of Civil and Environmental Engineering, Western New England University, Springfield, MA 01119, USA. Email: seunghee.kim@wne.edu. Tel:+1 413-782-1653. Fax: +1 413-796-2116.

Geofluids (2016) **16**, 329–341

INTRODUCTION

Carbon dioxide (CO_2) injection into geological formations, either for enhanced oil recovery or for CO_2 geological storage, triggers a complex cascade of interconnected events that may include CO_2 advection (Saripalli & McGrail 2002; Nordbotten *et al.* 2005; Ennis-King & Paterson 2007), buoyancy (Bachu & Adams 2003; Bielinski *et al.* 2008; Okwen *et al.* 2010), convection of CO_2-dissolved water (Weir *et al.* 1996; Riaz *et al.* 2006; Hassanzadeh *et al.* 2007; Kneafsey & Pruess 2010), mutual diffusion and dissolution between CO_2 and the water phase and salt precipitation (Gaus *et al.* 2005; Berne *et al.* 2010; Espinoza & Santamarina 2010; Li *et al.* 2011), viscous fingering of CO_2 (Homsy 1987; Fenghour *et al.* 1998; Cinar *et al.* 2009), and capillary trapping of the CO_2 phase by the water-saturated porous formation (Juanes *et al.* 2006; Kopp *et al.* 2009; Saadatpoor *et al.* 2009; Kim 2012). Furthermore, water acidification follows CO_2 dissolution and triggers reactions with minerals in the formation as well as with the cement around wells (Li *et al.* 2008; Solomon *et al.* 2008; Szymczak & Ladd 2009; Espinoza *et al.* 2011).

Reactive fluid transport generates positive feedbacks through hydro-chemo-mechanical couplings that may lead to emergent phenomena such as the formation of dissolution wormholes (Golfier *et al.* 2002; Berrezueta *et al.* 2013; Elkhoury *et al.* 2013; Hao *et al.* 2013; Mangane *et al.* 2013) and shear fractures in compression (Shin *et al.* 2008; Shin & Santamarina 2009). The mineral dissolution rate is scale dependent, and pseudo-kinetic issues must be considered when upscaling geochemical equilibrium

(Binning & Celia 2008; Li *et al.* 2008). Studies of reactive fluid transport in the context of CO_2 injection have addressed the geological formation (Flukiger & Bernard 2009; Molins *et al.* 2012; Hao *et al.* 2013; Ovaysi & Piri 2013, 2014; Steefel *et al.* 2013), consequences on wellbores (Raoof *et al.* 2012; Brunet *et al.* 2013; Cao *et al.* 2013; Patel *et al.* 2014), and changes in fracture properties and injectivity (Wang & Gu 2011; Jafari Behbahani *et al.* 2012; Smith *et al.* 2012; Deng *et al.* 2013).

This study develops a geometry-coupled numerical model to study reactive fluid transport at the fracture scale, including the ensuing interactions between reactions, transport, and pore enlargement. Note that previous coupled models have explored hydro-chemical conditions but have not captured geometric changes, e.g. Li *et al.* (2008) and Binning & Celia (2008); pore enlargement is a precursor for fully coupled hydro-chemo-mechanical coupling. In particular, we implement all reactions needed to analyze CO_2-rich water transport under conditions that would develop in the context of CO_2 geologic storage and enhanced oil recovery in fractured media. The goal is to advance our understanding of the flow of CO_2-dissolved water at the fracture scale as water rich in total carbonic acid H_2CO_3* and hydrogen ions H^+ traverses the fracture. We summarize transport patterns in terms of key dimensionless numbers to facilitate the analyses of fracture networks subjected to reactive fluid transport and ensuing pore enlargements. Kinetic rates are analyzed first followed by a 2D numerical simulation study of CO_2-dissolved water injection.

KINETIC RATES

CO_2 dissolution in water

Injected carbon dioxide CO_2 dissolves in the formation water or brine to sequentially form aqueous carbon dioxide $CO_{2(aq)}$ and carbonic acid H_2CO_3, which eventually dissociates into bicarbonate ions HCO_3^- and hydrogen ions H^+ (see details in the Appendix A). Assuming that the reaction rate is linearly proportional to the concentration of reactants (Eqs A.1 to A.3 in Appendix A), the following kinetic laws are obtained:

$$\frac{d[CO_{2(g)}]}{dt} = -k_g[CO_{2(g)}] + k_{aq}[CO_{2(aq)}] \quad (1)$$

$$\frac{d[CO_{2(aq)}]}{dt} = k_g[CO_{2(g)}] - k_{aq}[CO_{2(aq)}] - k_{CO_2}[CO_{2(aq)}] + k_{H_2CO_3}[H_2CO_3] \quad (2)$$

$$\frac{d[H_2CO_3]}{dt} = k_{CO_2}[CO_{2(aq)}] - k_{H_2CO_3}[H_2CO_3] - k_{12}[H_2CO_3] + k_{21}[HCO_3^-][H^+] \quad (3)$$

$$\frac{d[H^+]}{dt} = \frac{d[HCO_3^-]}{dt} = k_{12}[H_2CO_3] - k_{21}[HCO_3^-][H^+] \quad (4)$$

where square brackets around species indicate species concentrations. Rate constants k_i in Eqs 1–4 are summarized in Table 1.

We can numerically examine the evolution of species concentrations with these kinetic rate laws. For instance, the solution of differential Eqs 1–4 (using fourth-order Runge–Kutta method) shows that the concentration of hydrogen ions in water $[H^+]$ converges to $10^{-3.28}$ mol l^{-1} and the acidity level drops to pH ≈ 3.28 at steady state (under a partial pressure of P_{CO2} = 10 MPa and temperature T = 40°C).

Mineral dissolutions

Geological formations typically considered for CO_2 storage are sandstones and carbonates (Bachu *et al.* 1994). Then, we analyze two representative minerals: calcite $CaCO_3$ (fast dissolution) and anorthite $CaAl_2Si_2O_8$ (slow dissolution). Dissolution rates in the presence of CO_2-dissolved water are analyzed next.

Calcite Dissolution

Three concurrent chemical reactions take place when calcite is in contact with CO_2-acidified water, each with its own rate constant k_i and equilibrium constant K_{eq} (Plummer *et al.* 1978):

$$CaCO_{3(s)} + H^+ \xrightarrow{k_1} Ca^{2+} + HCO_3^-; \quad \log K_{eq} = 1.85 \quad (5)$$

$$CaCO_{3(s)} + CO_{2(aq)} + H_2O \xrightarrow{k_2} Ca^{2+} + 2HCO_3^-; \quad \log K_{eq} = -4.50 \quad (6)$$

$$CaCO_{3(s)} \xrightarrow{k_3} Ca^{2+} + CO_3^{2-}; \quad \log K_{eq} = -8.48 \quad (7)$$

The first reaction consumes one mole of H^+ and produces one mole of Ca^{2+} and one mole of HCO_3^- (Eq. 5). The second reaction consumes one mole of $CO_{2(aq)}$ in exchange for one mole of Ca^{2+} and two moles of HCO_3^- (Eq. 6). The last reaction (Eq. 7) has much smaller rate and equilibrium constants, and it is ignored in the numerical simulation (note: Rate constants are listed in Table 1). The overall dissolution rate R_d is estimated as follows (transition state theory—Lasaga 1984; Li *et al.* 2008):

$$R_d = \left(k_1[H^+] + k_2[CO_{2(aq)}]\right)\left(1 - \frac{\Omega}{K_{tot}}\right), \quad \text{where } \Omega = \frac{[Ca^{2+}]^2[HCO_3^-]^3}{[H^+][CO_{2(aq)}]} \quad (8)$$

Note that Ω at equilibrium is equal to the overall equilibrium constant; $\log K_{tot}$ = 1.85–4.50 = −2.65 (refer to Eqs 5 and 6; Table 1).

Table 1 Parameters used in simulations.

CO_2 kinetic		
k_g	5×10^{-3} sec^{-1} (1)	Rate constant of $CO_{2(g)} \rightarrow CO_{2(aq)}$
k_{aq}	k_g / K_H (1)	Rate constant of $CO_{2(g)} \leftarrow CO_{2(aq)}$
k_{CO_2}	0.135 sec^{-1} (2)	Rate constant of $CO_{2(aq)} \rightarrow H_2CO_3$
$k_{H_2CO_3}$	72.982 sec^{-1} (2)	Rate constant of $CO_{2(aq)} \leftarrow H_2CO_3$
k_{12}	10^7 sec^{-1} (3)	Rate constant of $H_2CO_3 \rightarrow H^+ + HCO_3^-$
k_{21}	4.1×10^{10} sec^{-1} (3)	Rate constant of $H_2CO_3 \leftarrow H^+ + HCO_3^-$
K_H	$10^{-1.64}$ (2)	Henry's constant at 40°C
Calcite fracture plane		Anorthite fracture plane
$[H^+]_{inlet}$	10^{-6}–10^{-3} mol l^{-1}	$[H^+]_{inlet}$ 10^{-6}–10^{-3} mol L^{-1}
$[H_2CO_3^*]_{inlet}$	10^{-3}–1 mol l^{-1}	$[H_2CO_3^*]_{inlet}$ 10^{-3}–1 mol l^{-1}
$[Ca^{2+}]_{inlet}$	1.36×10^{-3} mol l^{-1} (4)	$[HCO_3^-]_{inlet}$ 6.68×10^{-4} mol l^{-1} (4)
$[HCO_3^-]_{inlet}$	6.68×10^{-4} mol l^{-1} (4)	$[OH^-]_{inlet}$ 1.50×10^{-11} mol l^{-1} (4)
$[OH^-]_{inlet}$	1.50×10^{-11} mol l^{-1} (4)	$[Ca^{2+}]_{inlet}$ 2.11×10^{-4} mol l^{-1} (4)
$[Cl^-]_{inlet}$	2.72×10^{-3} mol l^{-1} (4)	$[Al^{3+}]_{inlet}$ 3.51×10^{-8} mol l^{-1} (4)
		$[H_4SiO_4]_{inlet}$ 9.67×10^{-13} mol l^{-1} (4)
		$[Cl^-]_{inlet}$ 4.22×10^{-4} mol l^{-1} (4)
$[H^+]_{initial}$	1.0×10^{-8} mol l^{-1} (5)	$[H^+]_{initial}$ 1.0×10^{-8} mol l^{-1} (6)
$[H_2CO_3^*]_{initial}$	1.0×10^{-5} mol l^{-1} (5)	$[H_2CO_3^*]_{initial}$ 1.0×10^{-5} mol l^{-1} (6)
$[Ca^{2+}]_{initial}$	1.59×10^{-3} mol l^{-1} (5)	$[HCO_3^-]_{initial}$ 4.47×10^{-4} mol l^{-1} (6)
$[HCO_3^-]_{initial}$	4.47×10^{-4} mol l^{-1} (5)	$[OH^-]_{initial}$ 1.0×10^{-6} mol l^{-1} (6)
$[OH^-]_{initial}$	1.0×10^{-6} mol l^{-1} (5)	$[Ca^{2+}]_{initial}$ 4.35×10^{-4} mol l^{-1} (6)
$[Cl^-]_{initial}$	2.72×10^{-3} mol l^{-1} (5)	$[Al^{3+}]_{initial}$ 3.51×10^{-8} mol l^{-1} (6)
		$[H_4SiO_4]_{initial}$ 9.67×10^{-13} mol l^{-1} (6)
		$[Cl^-]_{initial}$ 4.22×10^{-4} mol l^{-1} (6)
k_1	0.745 mol m^{-2} sec^{-1} (7)	k_H 3.4×10^{-4} mol m^{-2} sec^{-1} (8)
k_2	8.6×10^{-4} mol m^{-2} sec^{-1} (7)	k_{H2O} 1.8×10^{-12} mol m^{-2} sec^{-1} (8)
K_{tot}	$10^{-2.65}$ (7)	K_{tot} $10^{21.7}$ (8)
v_0	10^{-3}–1 cm sec^{-1}	Inlet velocity
η	10^{-3} Pa·s	Viscosity of fluid
ρ_f	1100 kg m^{-3}	Density of fluid
S_s	0.06 m^2 g^{-1} (9)	Specific surface of calcite and anorthite
M_m	100 g mol^{-1}	Molar mass of calcite
	277 g mol^{-1}	Molar mass of anorthite
V_m	3.7×10^{-5} m^3 mol^{-1}	Molar volume of calcite
	10.1×10^{-5} m^3 mol^{-1}	Molar volume of anorthite
D	2.0×10^{-9} m^2 sec^{-1}	Average diffusion coefficient for all species

Rate constants are computed for temperature T = 40°C. References are from: (1) Sposito (1994), (2) Stumm *et al.* (1996), (3) Zhang (2008); species concentrations are examples computed for (4) pH = 3.18, (5) pH = 8 and $K_{tot} = 10^{-2.65}$, (6) pH = 8 and $K_{tot} = 10^{21.7}$; (7) Renard *et al.* (2005); Wigand *et al.* (2008); Algive *et al.* (2009), (8) Li *et al.* (2006), (9) Gaus *et al.* (2005).

Anorthite Dissolution

We adopt the model by Li *et al.* (2006) to represent the dissolution of anorthite. The reaction consumes eight moles of H^+ to produce one mole of Ca^{2+}, two moles of Al^{3+}, and two moles of H_4SiO_4:

$$CaAl_2Si_2O_{8(s)} + 8H^+ \xrightarrow{k_H} Ca^{2+} + 2Al^{3+} + 2H_4SiO_4 \qquad (9)$$

Again, the overall dissolution rate is described as a function of rate constants, concentrations of reactant species, and saturation:

$$R_d = \left(k_H[H^+]^{1.5} + k_{H_2O} + k_{OH}[OH^-]^{0.33}\right)\left(1 - \frac{\Omega}{K_{tot}}\right),$$
$$\text{where } \Omega = \frac{[Ca^{2+}][Al^{3+}]^2[H_4SiO_4]^2}{[H^+]^8} \qquad (10)$$

Rate constants and equilibrium constant are compiled in Table 1. We disregard the term $k_{OH}[OH^-]^{0.33}$ during the numerical simulation because both the rate constant and the concentration of hydroxide $[OH^-]$ are negligible.

Figure 1 compares the overall 'local' mineral dissolution rate R_d for a fixed concentration of the total carbonic acid H_2CO_3* at $[H_2CO_3^*] = 1$ mol l^{-1}. Results show that the concentration of hydrogen ions $[H^+]$ controls the reaction rate of calcite when pH≤~4 (thereafter, the high concentration of total carbonic acid $[H_2CO_3^*]$ takes control), and the reaction rate of anorthite when pH≤~6. The reaction rate of calcite is several orders of magnitude higher than that of anorthite when 2 < pH < 7 (Fig. 1).

NUMERICAL SIMULATION OF REACTIVE FLUID FLOW

The coupling between hydro-chemical phenomena during the transport of reactive CO_2-acidified water through a pore or fracture in a mineral system is investigated next. We start by identifying the governing dimensionless ratios.

Dimensionless ratios

Consider a reactive fluid advecting with velocity v [m sec^{-1}] through a rock fracture driven by a pressure difference between inlet and outlet boundaries at a distance l [m] from each other. Reactant species are transported toward the mineral surface by molecular diffusion so that the fracture aperture d [m] and the diffusion coefficient D [m^2 sec^{-1}] determine the characteristic time for transverse diffusion. Mineral dissolution at the fracture surface produces species that are carried away by both advection (downstream) and diffusion (in all directions).

Three dimensionless ratios capture the interplay between governing processes. The Damköhler number Da is the ratio between the advection time and the chemical reaction time (Fredd & Fogler 1998).

$$Da = \frac{t_{\text{advection}}}{t_{\text{reaction}}} = \frac{\kappa l}{v} \tag{11}$$

where the kinetic rate κ [1/sec] = $k_r \cdot S_s \cdot M_m$ is a function of the rate constant for mineral dissolution k_r [mol m^{-2} sec^{-1}], the mineral specific surface S_s [m^2 g^{-1}], and the mineral molar mass M_m [g mol^{-1}]. The Peclet number compares the time for either transverse $Pe^{\perp}$ or longitudinal $Pe^{//}$ diffusion to the time for longitudinal advection (Golfier *et al.* 2002):

$$Pe^{\perp} = \frac{t^{\perp}_{\text{diffusion}}}{t_{\text{advection}}} = \frac{\mathrm{d}^2 v}{4lD} \quad \text{and} \quad Pe^{//} = \frac{t^{//}_{\text{diffusion}}}{t_{\text{advection}}} = \frac{lv}{D} \tag{12}$$

Simulation method—environment

Consider the plane across a rock fracture with length l much longer than the aperture d, that is, $l \gg d$, subjected to reactive fluid transport by the forced advection of CO_2-acidified water. The problem is simulated using the moving mesh function in COMSOL to reproduce the fracture enlargement due to chemical reaction (COMSOL 2008). Figure 2 summarizes the simulation scheme. Flow satisfies the Navier-Stokes law (Equation A in Fig. 2); species experience both advective and diffusive transport (Equation B in Fig. 2). Mineral dissolution occurs at the interface between the fluid and the fracture walls with dissolution rate R_d as predicted by Eq. 8 (calcite) or Eq. 10 (anorthite). In the fracture, species undergo homogeneous reactions as predicted by Eqs 1–4. The moving mesh function adjusts the mesh outward according to the volume of dissolved mineral $R_d \cdot (\upsilon_s \upsilon^{-1}) \cdot V_m$ [m sec^{-1}], where $(\upsilon_s \upsilon^{-1})$ denotes the stoichiometric ratio of dissolved mineral to reactant species and V_m [m^3 mol^{-1}] is the molar volume of the mineral (Equation C in Fig. 2).

Equations A, B, and C in Fig. 2 are fully coupled within the finite-element formation (linear system solver: Direct (PARDISO)—COMSOL 2008). The model consists of 1,608 triangular elements with maximum resolution around the inlet. A constant fluid injection velocity v_0 is imposed at the inlet of the fracture plane (Fig. 2). Note that Reynolds number $Re = \rho v_0 l / \eta$ needs to be checked to ensure that laminar flow conditions apply (values remain within $10^{-2} \le Re \le 10^{1}$ in this study). The nonpervious rock blocks that define the fracture are fixed in the far field, that is, zero-strain boundaries, and the fracture planes move out in accordance with mineral dissolution. Species concentrations at the inlet remain constant and correspond to CO_2 and H_2O in thermodynamic equilibrium. The initial concentration of all species in the fracture plane corresponds to the system in thermodynamic equilibrium and satisfies electro-neutrality at pH = 8. Numerical computations continue until the total simulation time equals 10

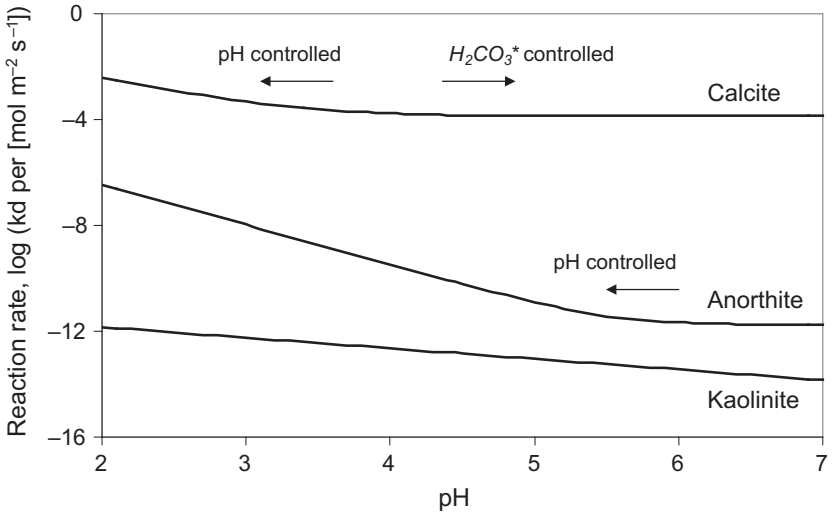

Fig. 1. Reaction rate $\log(k_d/[\text{mol m}^{-2}\ \text{sec}^{-1}])$ for the dissolution of calcite $CaCO_3$ and anorthite $CaAl_2Si_2O_8$ at a temperature T = 40°C and for a fixed concentration of total dissolved carbon dioxide $[H_2CO_3^*]$ = 1 mol l^{-1}. For comparison, the reaction rate is also plotted for kaolinite $Al_2Si_2O_5(OH)_4$ as a representative clay mineral of low reactivity; in this case, $k_d = k_H[H^+]^{0.4} + k_{OH}[OH^-]^{0.3}$, where k_H = 2.79 × 10^{-11} mol m^{-2} sec^{-1} and k_{OH} = 3.51 × 10^{-16} mol m^{-2} sec^{-1} at T = 40°C (Li *et al.* 2006).

times the advection time $10 \cdot l/v_0$ and involve more than 1000 time steps. All parameters used for numerical simulations are summarized in Table 1.

Validation

There is no analytical solution for reactive fluid transport in a two-dimensional pore. Instead, we compare the analytical solution for one-dimensional geometry with 1D numerical results obtained using the formulation described above. The governing equation for the one-dimensional transport of a reactive fluid is:

$$\frac{\partial c}{\partial t} = D\frac{\partial^2 c}{\partial x^2} - v\frac{\partial c}{\partial x} - \kappa c \tag{13}$$

For a single reactant species at an initial concentration $c(x,0) = 0$ for $x > 0$ and boundary conditions $c(0,t) = c_0$ and $c(\infty,t) = 0$ for $t \geq 0$, the solution for the variation of the species concentration in space and time is (Boudreau 1997) as follows:

$$\begin{aligned}\frac{c}{c_0} &= \frac{1}{2}\exp(\xi_2)\left[\exp(-\xi_1)erfc\left(\frac{2\xi_1 - \tau}{2\sqrt{\tau}}\right)\right. \\ &\quad \left. + \exp(\xi_1)erfc\left(\frac{2\xi_1 + \tau}{2\sqrt{\tau}}\right)\right] \\ \text{where } \beta^2 &= \left(\frac{v^2}{4D^2} + \frac{\kappa}{D}\right),\ \xi_1 = \beta x, \xi_2 = \frac{vx}{2D}, \\ \tau &= \frac{(v^2 + 4\kappa D)t}{D}\end{aligned} \tag{14}$$

Figure 3 shows that the 1D numerically computed concentrations are in agreement with the analytical results with minor derivations near the outlet. Two outlet boundary conditions are simulated to compare the finite-length numerical system with the infinite-length analytical solution: (i) free flux and (ii) fixed outlet concentration $c(l, t) = 0$. Numerical results bound the theoretical solution

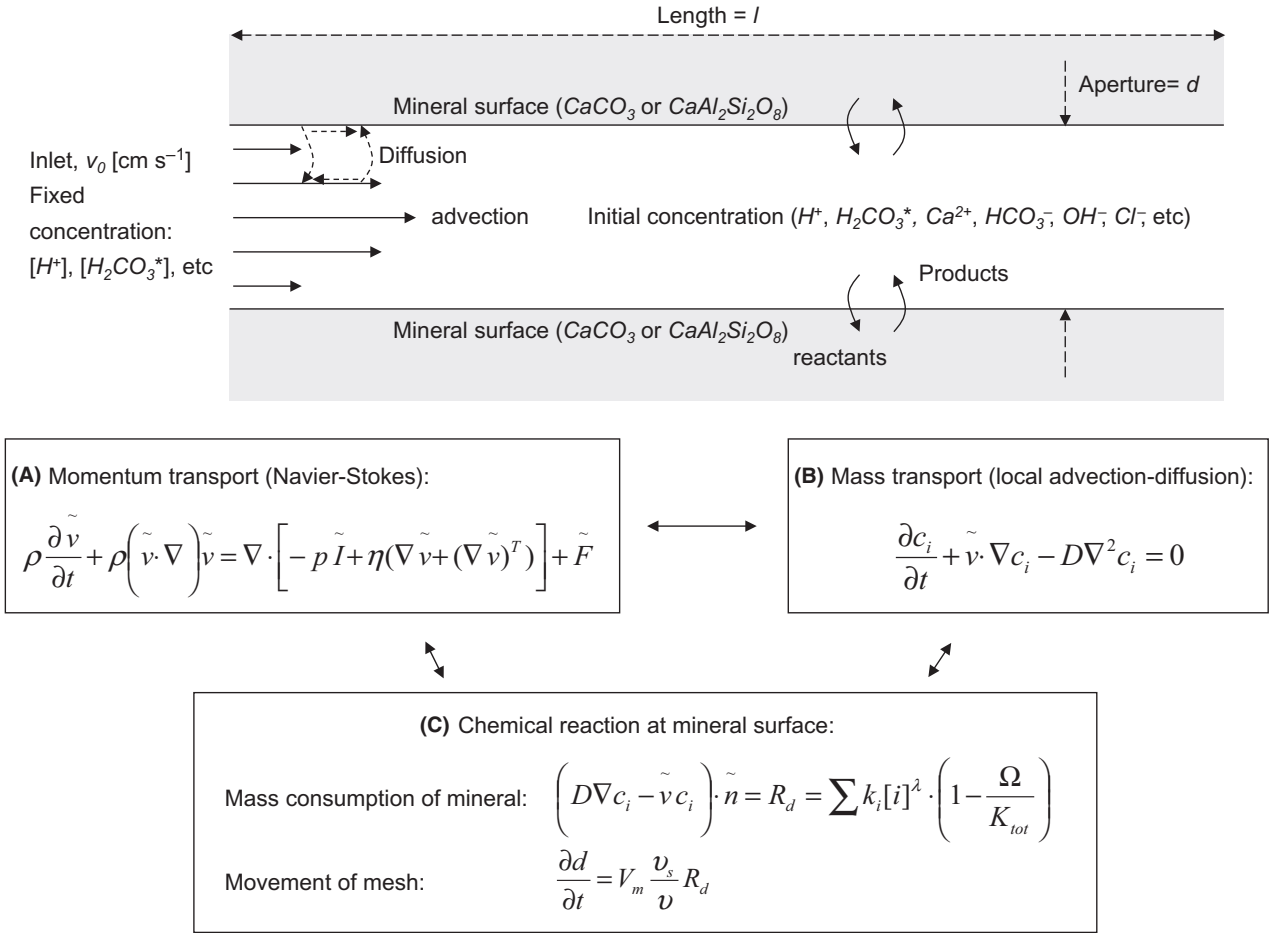

Fig. 2. Numerical simulation scheme and governing equations for reactive fluid flow through a rock pore/fracture. Physics models used in COMSOL: (A) incompressible Navier-Stokes (η: dynamic viscosity of fluid, ρ: density of fluid, $\tilde{v}$: velocity field, p: pressure, $\tilde{F}$: volume force field such as gravity; gravity is disregarded in the simulation), (B) advection and diffusion (c_i: concentration of species i, D: coefficient of molecular diffusion), and (C) moving mesh (R_d: overall dissolution rate of mineral at the wall, k_i: reaction rate of reactant species i, $[i]$: concentration of reactant species i, Ω: ionic concentration product, K_{tot}: equilibrium constant, d: fracture aperture, V_m: mineral molar volume, υ_s / υ: stoichiometric ratio between reactant species and dissolved mineral).

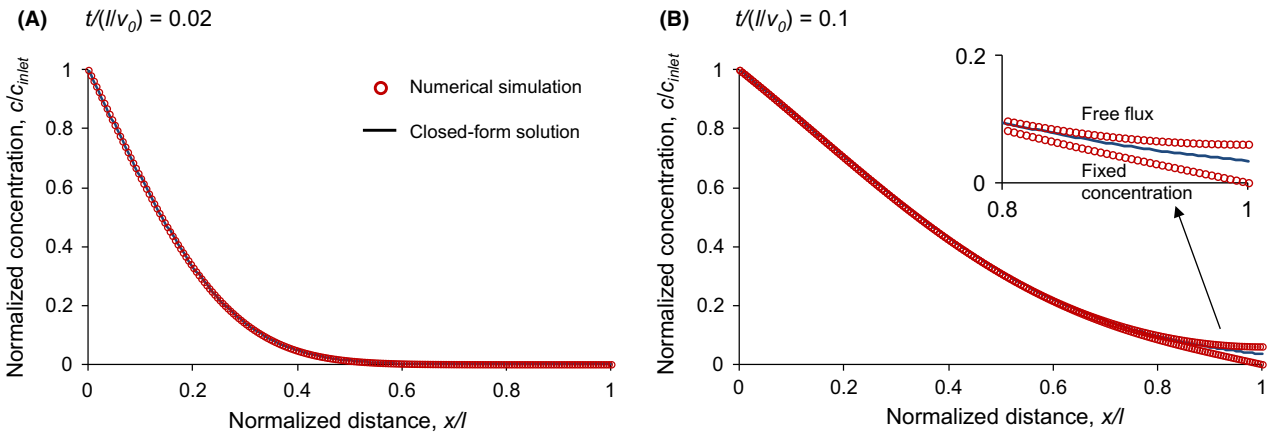

Fig. 3. Code validation: Comparison between numerical simulation results and values predicted using the closed-form solution for 1D reactive solute transport problem. Assumptions: homogeneous reaction of single species c_A for reaction $C_A \xrightarrow{k_{AB}} C_B$, where $k_{AB} = 0.1$ sec^{-1}. The insert in pane-b shows the discrepancy between the closed-form solution for the infinitely long tube and the numerical solution for a finite tube with two boundary conditions: free flux and fixed initial concentration at the outlet. Fixed inlet concentration of c_A $[c_A]_{(0,t)} = 1$ mol l^{-1}, initial concentration of c_A $[c_A]_{(x>0)} = 0$, fixed inlet velocity $v_0 = 0.01$ cm sec^{-1}, diffusion coefficient $D = 2 \times 10^{-9}$ m^2 sec^{-1}.

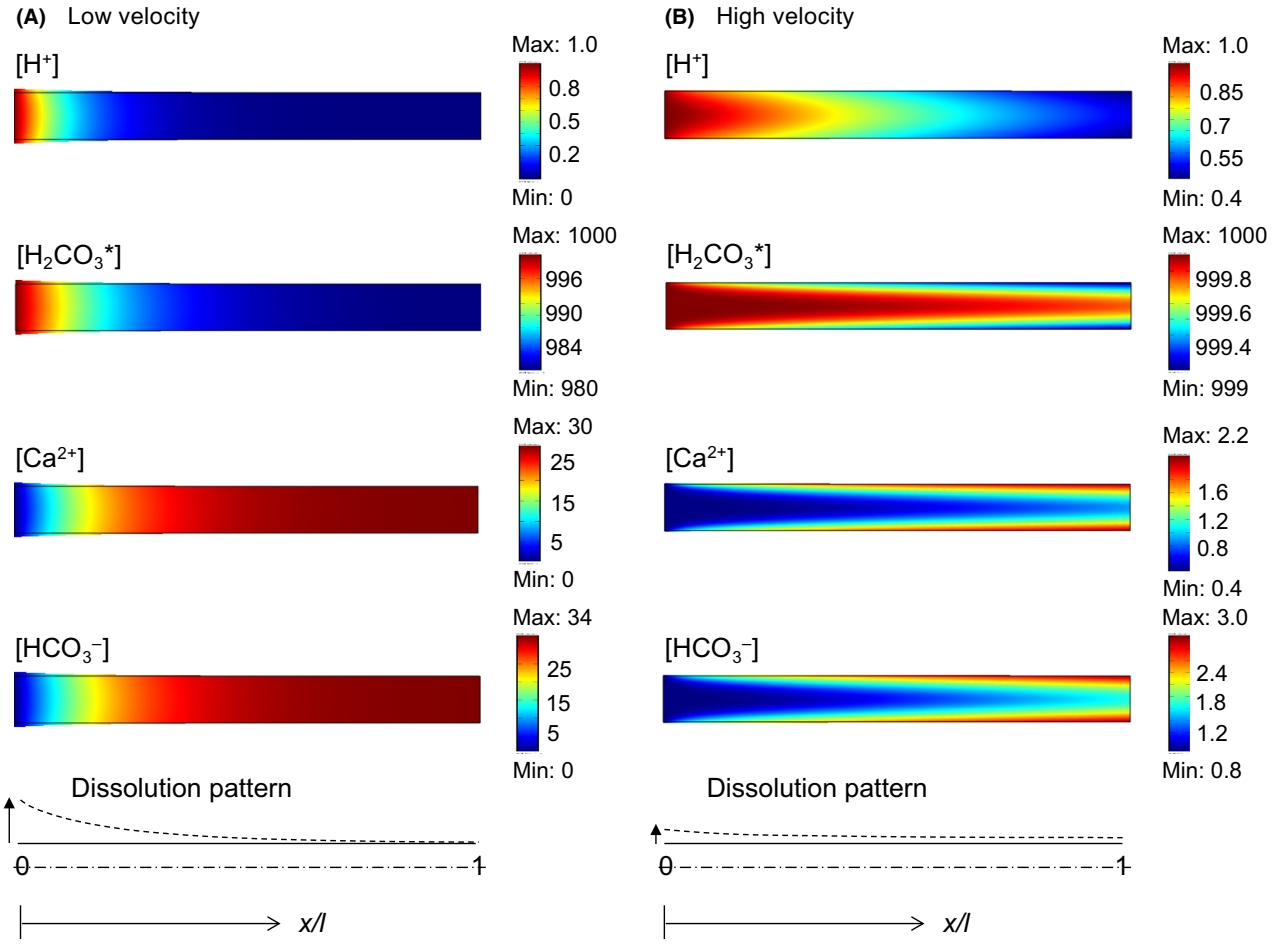

Fig. 4. Reactive fluid transport along a fracture in calcite. Concentration of reactants [H$^+$] and [H_2CO_3*], and produced species [Ca^{2+}] and [HCO_3^-]. Dimensionless numbers are as follows: (A) $Da \approx 10^2$ and $Pe^{\perp} \approx 3 \times 10^{-4}$ and (B) $Da \approx 10^{-1}$ and $Pe^{\perp} \approx 3 \times 10^{-1}$. Concentration results are shown at dimensionless times: (A) $t = 5 \times (l/v_0)$ and (B) $t = 1000 \times (l/v_0)$. Species concentrations are in [mol m^{-3}]. All parameters are summarized in Table 1.

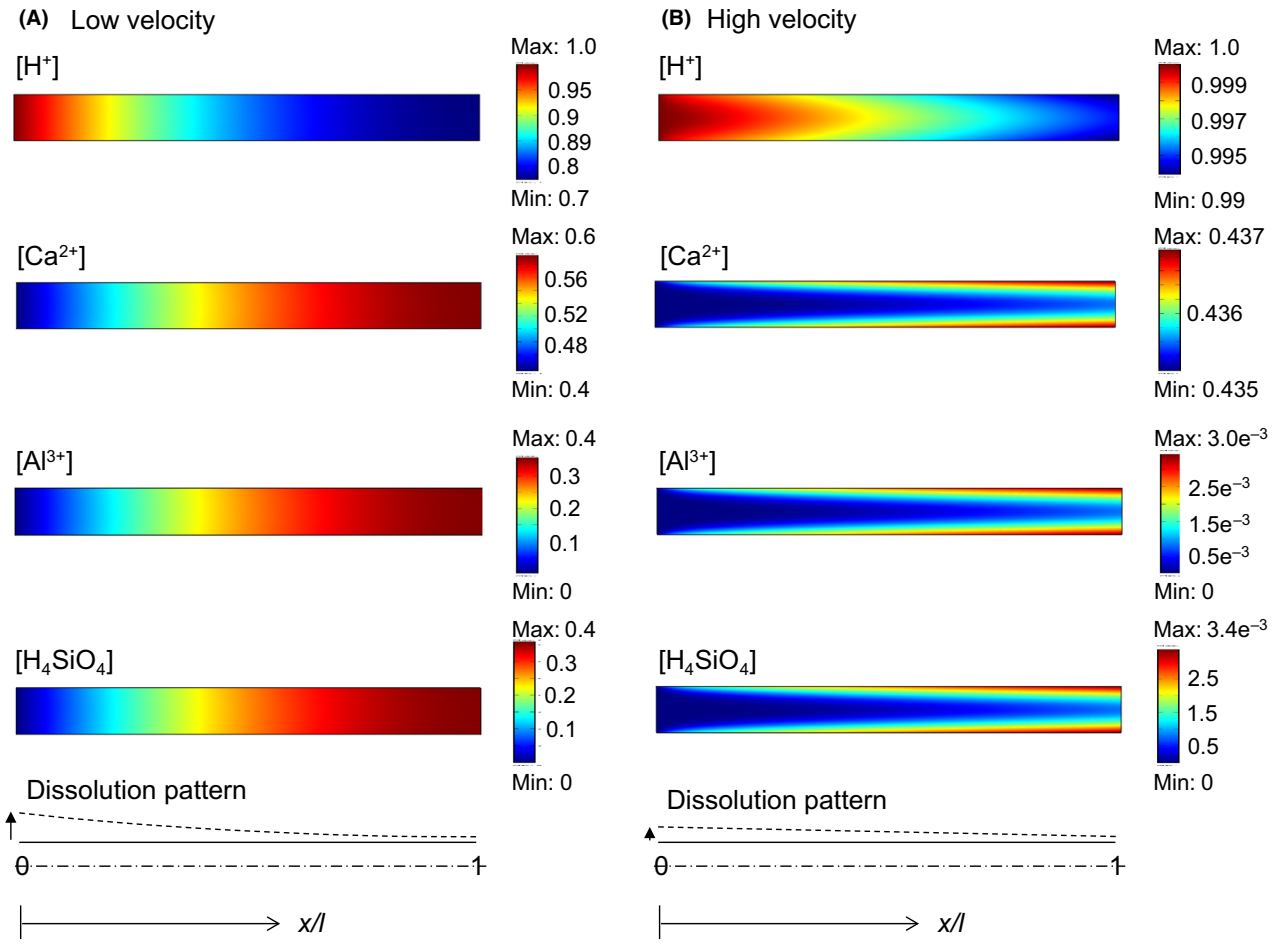

Fig. 5. Reactive fluid transport along a fracture in anorthite. Concentration of reactant [H^+], and produced species [Ca^{2+}], [Al^{3+}], and [H_4SiO_4]. Dimensionless numbers are as follows: (A) $Da \approx 6 \times 10^{-2}$ and $Pe^{\perp} \approx 3 \times 10^{-4}$ and (B) $Da \approx 6 \times 10^{-5}$ and $Pe^{\perp} \approx 3 \times 10^{-1}$. Concentrations are shown at dimensionless times: (A) $t = 0.5 \times (l/v_0)$ and (B) $t = 100 \times (l/v_0)$. Species concentrations are in [mol m^{-3}]. All parameters are summarized in Table 1.

(Fig. 3B). Electro-neutrality is maintained during the numerical simulation.

RESULTS AND DISCUSSION

Numerical simulation results for the 2D fracture case relevant to CO_2 geological storage are presented herein in terms of species concentrations in space and time, the enlargement of the rock fracture, and the morphing of the fracture geometry. Results are obtained for different regimes represented by dimensionless numbers *Da* and $Pe^{\perp}$.

Species concentration

For both mineralogies, a higher advection velocity (lower *Da*) yields higher concentrations of residual reactant species at the outlet due to the lower residence time. Thus, inlet species concentrations will influence deeper into the reservoir in anorthite. In particular:

(1) High *Da* ($> 10^{-1}$) *and Low* $Pe^{\perp}$*—Calcite.* Mineral dissolution couples with advection and diffusion to generate a concentration gradient across and along the pore/fracture aperture (for comparison, see Li *et al.* 2006). Figure 4 shows a snapshot of instantaneous concentrations for all relevant species along a fracture in calcite. Slow transverse diffusion and homogenization across the aperture develops at low advection velocity (low $Pe^{\perp}$) and leads to the large consumption of reactant species near the inlet (Fig. 4A). Clearly, H^+ is readily consumed, the system reaches chemical equilibrium, and H_2CO_3* passes through the rest of the fracture plane unconsumed in this calcite-dominant environment. The residual H_2CO_3* at the outlet may react with other minerals and induce additional mineral dissolution in successive flow channels.

(2) *High Da* ($> 10^{-1}$) *and high* $Pe^{\perp}$*—Calcite.* When the advection velocity is high, diffusion fails to homogenize the concentration field across the fracture (high

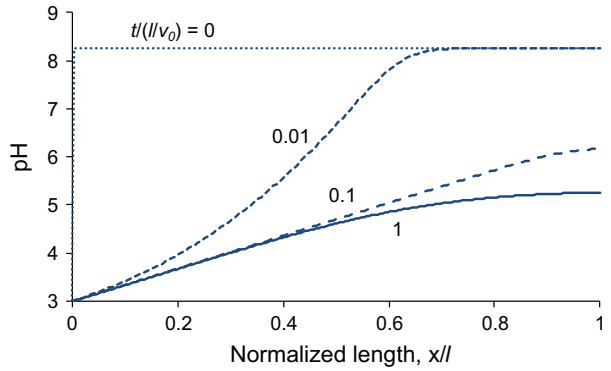

Fig. 6. Evolution of pH in time and space—anorthite. Values of pH along the length of fracture plane at selected normalized times $t/(l/v_0)$. *Note:* $Da \approx 6 \times 10^{-3}$ and $Pe^{\perp} \approx 3 \times 10^{-3}$. The pH distribution reaches quasi-steady state when $t/(l/v_0) > 1$.

$Pe^{\perp}$), and mineral dissolution is more uniform along the fracture length (Fig. 4B).

(3) *Low Da* ($< 10^{-1}$)—*Anorthite*. The longitudinal drop in reactant species is much lower in the less reactive anorthite for the same advection regimes (Fig. 5). The low reaction rate of H^+ with anorthite allows more than two-thirds of H^+ to reach the outlet unconsumed.

The fluid acidity evolves as the numerical simulation proceeds. During the early stages of acidified fluid flow along the rock fracture, the pH drops near the inlet and remains at the initial pH~8 toward the outlet. The entire pore space acidifies and the area near the outlet converges to an asymptotic value pH~5 as advection continues and the system becomes saturated in terms of mineral dissolution (Fig. 6).

Variations in reactant species concentrations along the fracture length are plotted in Fig. 7A at different normalized times $t/(l/v_0)$. The evolution of unconsumed reactants at the outlet is specifically explored in Fig. 7B for different $Pe^{\perp}$ values. Results show the evolution toward 'steady-state' reactive fluid flow.

Enlargement

The rock fracture aperture increases as the reactive fluid passes through the fracture plane (Figs 4 and 5). The effect of advective velocity and reactivity is explored in Figs 8 and 9. Results show that pore enlargement decreases along the flow path as reactants become consumed (primarily next to the fluid–rock interface) and

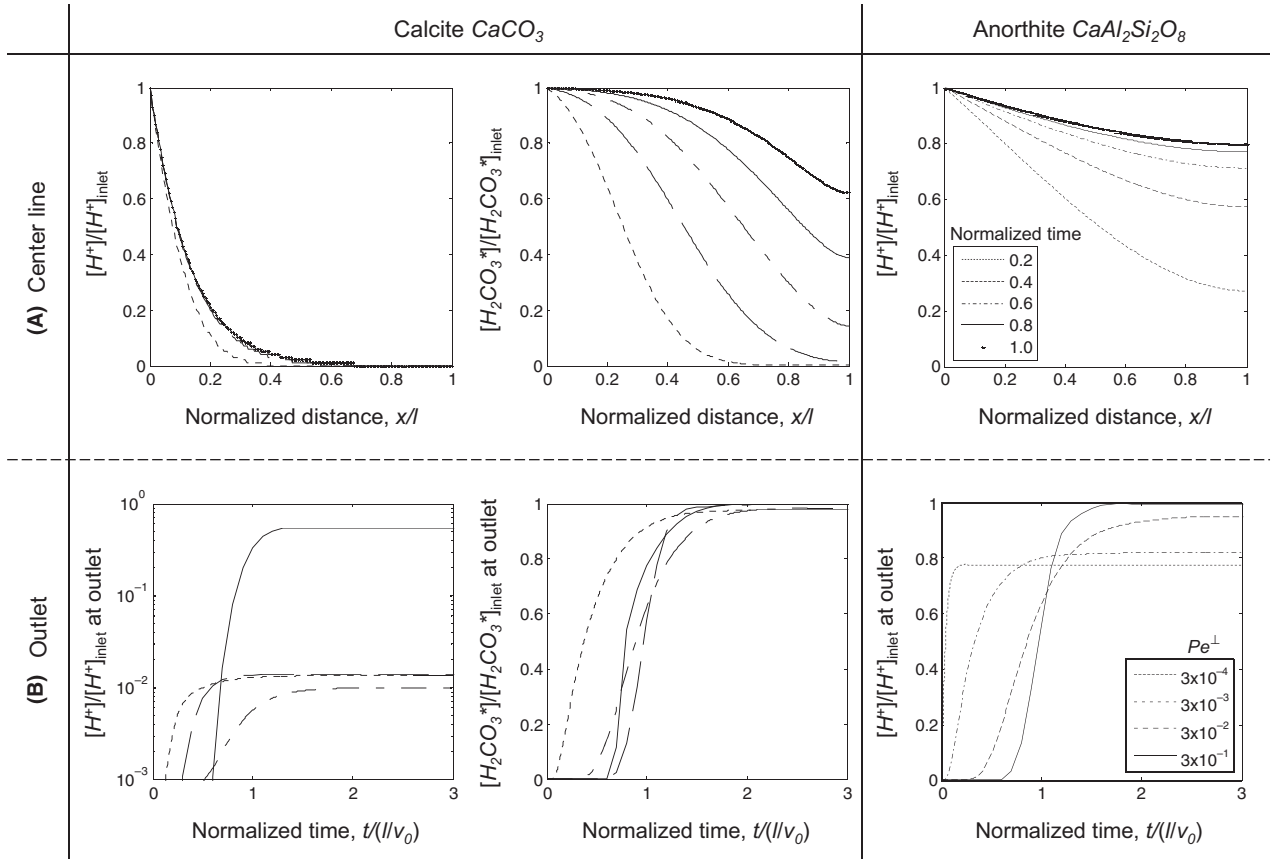

Fig. 7. Variation of reactant species concentration: (A) along the centerline for different normalized times ($Da \approx 10$ for calcite and $Da \approx 6 \times 10^{-3}$ for anorthite) and (B) at the outlet for different transverse Peclet numbers $Pe^{\perp}$. All parameters are summarized in Table 1.

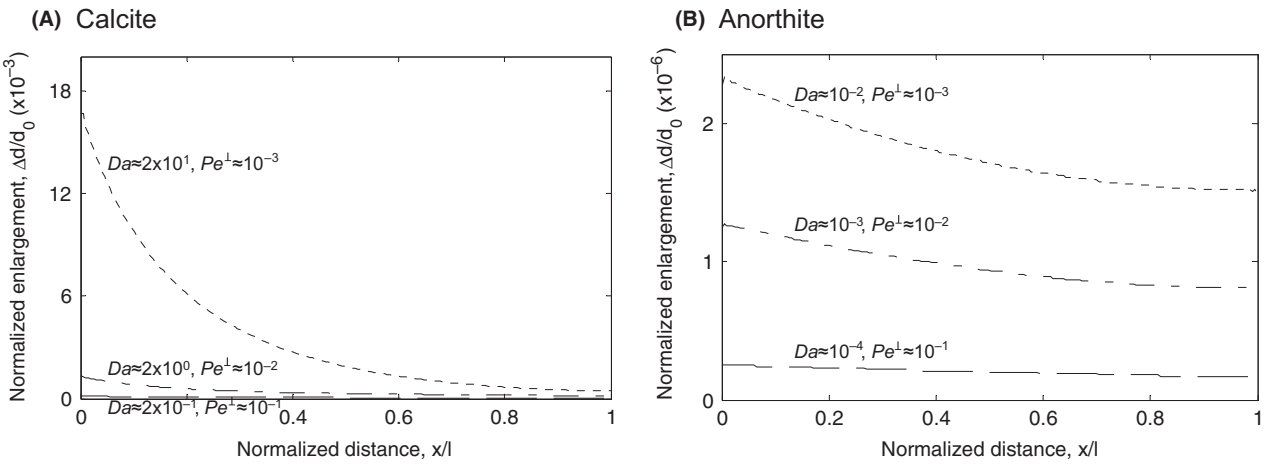

Fig. 8. Normalized aperture enlargement $\Delta d/d_0$ due to mineral dissolution along the fracture wall at the moment of quasi-steady-state concentration conditions for different *Da* and $Pe^{\perp}$ values and for a fracture slenderness $l/d = 10$. (A) Calcite. (B) Anorthite. Note: Orders of enlargement are different between the results for the two minerals. In all the cases shown, steady-state conditions were reached with <2 pore volumes of flow through (refer to Fig. 10).

aqueous species concentration approaches equilibrium. In all the cases, the normalized enlargement $\Delta d/d$ in anorthite is three orders of magnitude smaller than that of calcite at comparable times and flow regimes (Fig. 8—note: Steady-state conditions were reached with less than 2 pore volumes of flow through in all these cases).

Figure 9 compiles the observed evolving morphology in terms of dimensionless numbers, *Da* and $Pe^{\perp}$. At a given $Pe^{\perp}$, a lower *Da* causes the flow channel to experience a more uniform enlargement of the aperture along the fracture.

Time to reach quasi-steady-state condition

The time to reach quasi-steady-state concentration at the outlet t_{qc} is determined when species concentrations at the outlet c reach 95% of the equilibrium values c_∞ at $t = \infty$ (refer to Fig. 7B). Figure 10A,B indicates that the time to reach quasi-steady state t_{qc} for a fracture $l/d = 10$ is related to the advection time l/v_0 through *Da* and $Pe^{\perp}$ numbers.

The dimensionless time $t/(l/v_o)$ equals the number of pore volumes that have traversed the fracture. At $Pe \ll 1$, homogenization is diffusion-controlled and can be reached without

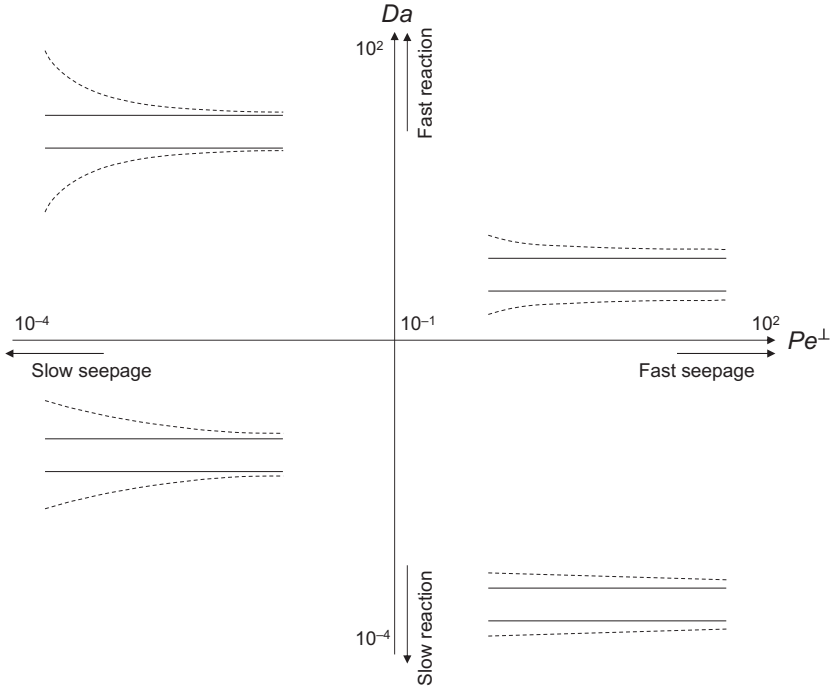

Fig. 9. Evolving fracture morphology in the *Da*–$Pe^{\perp}$ space. Sketches show dissolution patterns observed in numerical simulations of fractures with initially parallel planes. Trends shown in this dimensionless plot apply to both calcite and anorthite.

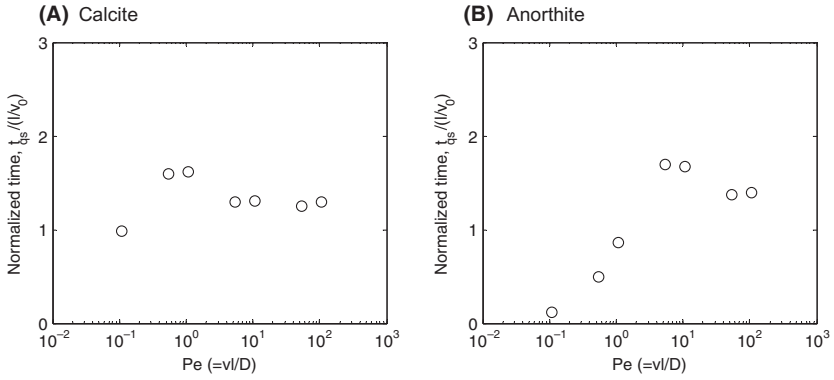

Fig. 10. Time to reach quasi-steady-state concentration t_{qs} at the outlet (95% of c/c_{∞}, where the equilibrium value c_{∞} is at $t = \infty$). (A) Calcite ($Da = 10^{-1}$~10^{2}) and (B) anorthite ($Da = 6 \times 10^{-5}$~6×10^{-2}). *Note:* The time t_{qs} is normalized by the advection time l/v_0 based on the fracture length l and the initial velocity v_0; for an alternative interpretation, consider the normalized time $t_{qs}/(l/v_o)$ as the number of pore volumes flushed through the fracture to reach steady state.

flow, hence $t/(l/v_o) \rightarrow 0$. Near $Pe \approx 1$ (depends on Da), counter-flow diffusion delays the time to reach quasi-steady state, and the largest number of pore volumes is required to steady state: $t/(l/v_o)$ approaches ≈ 2 (Fig. 10A,B). Finally, mineral dissolution and channel enlargement combine to extend the time to quasi-steady-state conditions beyond the advection time when $Pe \gg 1$, and the number of pore volumes required exceeds $t/(l/v_o) = 1$.

Initial fracture slenderness

Finally, let us examine the effect of fracture slenderness by varying the length-to-aperture ratio l/d; we keep Da constant by changing the initial aperture d. When the ratio l/d is large $l/d \geq 30$, transverse diffusive transport homogenizes species concentrations across the fracture, and centerline concentrations resemble the one-dimensional theoretical solution for the same advection velocity (Fig. 11). For the same length l, a wider aperture d slows the transverse diffusive transport of reactant species to the mineral surface ($t_{diff} \approx d^2/D$), and higher reactant concentrations remain along the centerline (Fig. 11). Therefore, scaling must take into consideration both the fracture length and its slenderness (see also Li *et al.* 2008).

Let us examine a fracture network subjected to reactive fluid transport. If the length-to-aperture ratio of single fractures is large (i.e. $l/d \geq 30$), species concentration resembles a 1D problem in each fracture. Then, if $Pe \gg 1$ and $Da \ll 1$, fracture morphology evolves uniformly within each fracture (Fig. 9) and can be modeled with a uniform aperture evolution during reactive transport. Single fracture morphology would evolve with a pyramidal shape outside these conditions. In all the cases, steady-state conditions are reached with <2 pore volumes of flow

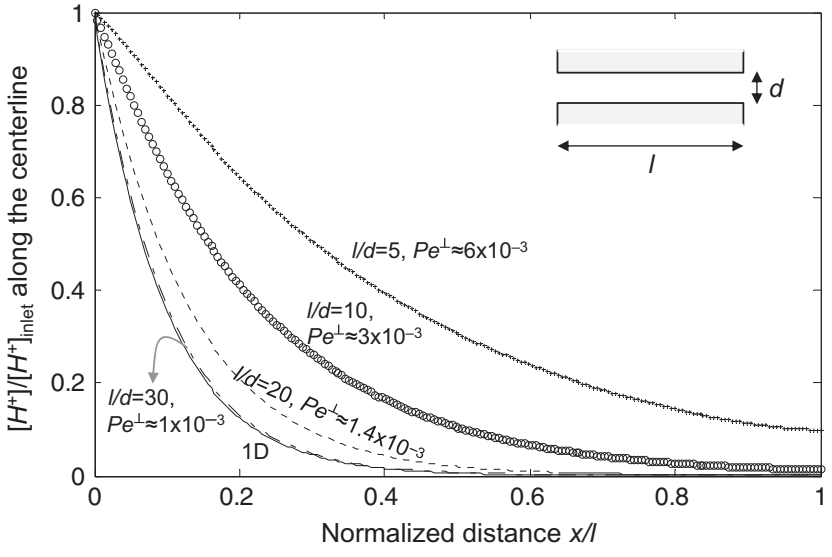

Fig. 11. Effect of the length-to-aperture ratio l/d for the same $Da \approx 10$. Variation of the normalized concentration of hydrogen ions $[H^+]/[H^+]_{inlet}$ at quasi-steady state for fractures in calcite with different slenderness. The theoretical 1D solution is shown for comparison. All parameters are summarized in Table 1.

through each fracture when constant inlet chemistry is involved; clearly, this is not the case in a fracture network. The situation is aggravated when highly reactive minerals are involved, such as in calcite as compared to anorthite, as much larger fracture enlargements will develop, other conditions being the same. In summary, fracture network analyses must consider both the length and slenderness of fractures, in addition to flow conditions captured in *Pe* and *Da*.

CONCLUSIONS

Reactive fluid transport through a rock fracture was simulated taking into consideration kinetic rate laws relevant to CO_2 injection for geological storage and enhanced oil recovery in calcite and anorthite, which affect both reservoirs and wells. The geometry-coupled numerical simulation combines laminar flow, advective and diffusive mass transport of species, mineral dissolution, and pore enlargement. Salient results follow.

Reactive fluid transport in a rock pore or fracture can be described in terms of two dimensionless parameters Damköhler *Da* and Peclet *Pe* numbers to take into consideration reactivity, advection, and diffusion.

In highly reactive low-advection conditions ($Da > 10^{-1}$ and low $Pe^{\perp}$—e.g. low advection velocity in calcite), hydrogen ions H^+ are readily consumed near the inlet, the fluid becomes saturated with reaction products, and H_2CO_3* traverses the rest of the fracture length unconsumed. When the advection velocity increases and $Pe^{\perp} > 10^{-1}$, diffusion fails to homogenize the concentration field across the fracture, and mineral dissolution takes place more uniformly along the fracture length.

In low reactivity cases ($Da < 10^{-1}$—anorthite), H^+ is further transported along the fracture. Low reactivity and *Da* values lead to a more uniform aperture enlargement along the length of the fracture at a given $Pe^{\perp}$. Therefore, the evolving morphology of the fracture depends on *Da* and $Pe^{\perp}$.

In general, mineral dissolution couples with pore enlargement to extend the time to reach quasi-steady state. In all the cases tested in this study, steady-state conditions for a single fracture subjected to constant inlet conditions are reached with <2 pore volumes of flow through.

Reactive fluid transport along a fracture resembles the 1D problem when the length-to-aperture ratio is large, say $l/d \geq 30$. For a given length l, an increased fracture aperture d slows the diffusive transport of reactant species to the mineral fracture surface, and higher reactant concentrations remain along the centerline. Therefore, fracture network analyses must take into consideration both the length and slenderness of individual fractures in addition to flow conditions captured in *Pe* and *Da*.

The numerical approach developed in this study can be extended to 3D fracture networks. Then, this mass-conserving model can be coupled with mechanical equilibrium and deformation compatibility to explore the response of fractured rock in the subsurface.

ACKNOWLEDGEMENTS

Support for this research was provided by the U. S. Department of Energy project DE-FE0001826. Any opinion, findings, conclusions, or recommendations expressed herein are those of the authors and do not necessarily reflect the views of funding organizations. A. Mezencevova's comments helped clarify the chemical analyses. F. J. Santamarina edited the original manuscript. This research was conducted while the authors were at Georgia Institute of Technology, Atlanta, USA.

REFERENCES

Algive L, Bekri S, Vizika-kavvadias O (2009) Reactive pore network modeling dedicated to the determination of the petrophysical property changes while injecting CO_2. In: *SPE Annual Technical Conference and Exhibition* New Orleans, Louisiana, USA, Society of Petroleum Engineers, 124305, 124305-MS.

Bachu S, Adams JJ (2003) Sequestration of CO_2 in geological media in response to climate change: capacity of deep saline aquifers to sequester CO_2 in solution. *Energy Conversion and Management*, **44**, 3151–75.

Bachu S, Gunter WD, Perkins EH (1994) Aquifer disposal of CO_2: hydrodynamic and mineral trapping. *Energy Conversion and Management*, **35**, 269–79.

Berne P, Bachaud P, Fleury M (2010) Diffusion properties of carbonated caprocks from the Paris Basin. *Oil & Gas Science and Technology-Revue De L Institut Francais Du Petrole*, **65**, 473–84.

Berrezueta E, González-Menéndez L, Breitner D, Luquot L (2013) Pore system changes during experimental CO_2 injection into detritic rocks: studies of potential storage rocks from some sedimentary basins of Spain. *International Journal of Greenhouse Gas Control*, **17**, 411–22.

Bielinski A, Kopp A, Schutt H, Class H (2008) Monitoring of CO_2 plumes during storage in geological formations using temperature signals: numerical investigation. *International Journal of Greenhouse Gas Control*, **2**, 319–28.

Binning PJ, Celia M (2008) Pseudokinetics arising from the upscaling of geochemical equilibrium. *Water Resources Research*, **44**, W07410.

Boudreau BP (1997) *Diagenetic Models and Their Implementation: Modelling Transport and Reactions in Aquatic Sediments.* Springer, Berlin.

Brunet J-PL, Li L, Karpyn ZT, Kutchko BG, Strazisar B, Bromhal G (2013) Dynamic evolution of cement composition and transport properties under conditions relevant to geological carbon sequestration. *Energy & Fuels*, **27**, 4208–20.

Cao P, Karpyn ZT, Li L (2013) Dynamic alterations in wellbore cement integrity due to geochemical reactions in CO_2-rich environments. *Water Resources Research*, **49**, 4465–75.

Cinar Y, Riaz A, Tchelepi HA (2009) Experimental study of CO_2 injection into saline formations. *SPE Journal*, **12**, 588–94.

COMSOL (2008) *COMSOL: Multiphysics Modeling and Engineering Simulation Software*. COMSOL, Stockholm, Sweden.

Deng H, Ellis BR, Peters CA, Fitts JP, Crandall D, Bromhal GS (2013) Modifications of carbonate fracture hydrodynamic properties by CO_2-acidified brine flow. *Energy & Fuels*, **27**, 4221–31.

Elkhoury JE, Ameli P, Detwiler RL (2013) Dissolution and deformation in fractured carbonates caused by flow of CO_2-rich brine under reservoir conditions. *International Journal of Greenhouse Gas Control*, **16**, S203–15.

Ennis-King J, Paterson L (2007) Coupling of geochemical reactions and convective mixing in the long-term geological storage of carbon dioxide. *International Journal of Greenhouse Gas Control*, **1**, 86–93.

Espinoza DN, Santamarina JC (2010) Water-CO_2-mineral systems: interfacial tension, contact angle, and diffusion—Implications to CO_2 geological storage. *Water Resources Research*, **46**, W07537.

Espinoza DN, Kim S, Santamarina JC (2011) CO_2 geological storage—Geotechnical implications. *KSCE Journal of Civil Engineering*, **15**, 707–19.

Fenghour A, Wakeham WA, Vesovic V (1998) The viscosity of carbon dioxide. *Journal of Physical and Chemical Reference Data*, **27**, 31–44.

Flukiger F, Bernard D (2009) A new numerical model for pore scale dissolution of calcite due to CO_2 saturated water flow in 3D realistic geometry: principles and first results. *Chemical Geology*, **265**, 171–80.

Fredd CN, Fogler HS (1998) Influence of transport and reaction on wormhole formation in porous media. *AIChE Journal*, **44**, 1933–49.

Gaus I, Azaroual M, Czernichowski-Lauriol I (2005) Reactive transport modelling of the impact of CO_2 injection on the clayey cap rock at Sleipner (North Sea). *Chemical Geology*, **217**, 319–37.

Golfier F, Zarcone C, Bazin B, Lenormand R, Lasseux D, Quintard M (2002) On the ability of a Darcy-scale model to capture wormhole formation during the dissolution of a porous medium. *Journal of Fluid Mechanics*, **457**, 213–54.

Hao Y, Smith M, Sholokhova Y, Carroll S (2013) CO_2-induced dissolution of low permeability carbonates. Part II: numerical modeling of experiments. *Advances in Water Resources*, **62**, 388–408.

Hassanzadeh H, Pooladi-Darvish M, Keith DW (2007) Scaling behavior of convective mixing, with application to geological storage of CO_2. *AIChE Journal*, **53**, 1121–31.

Homsy G (1987) Viscous fingering in porous media. *Annual Review of Fluid Mechanics*, **19**, 271–311.

IPCC (2005) IPCC special report on carbon dioxide capture and storage. In: *Prepared by Working Group III of the Intergovernmental Panel on Climate Change* (eds Metz B, Davidson O, de Coninck HC, Loos M, Meyer LA), pp. 442. Cambridge University Press, Cambridge, UK and New York.

Jafari Behbahani T, Ghotbi C, Taghikhani V, Shahrabadi A (2012) Investigation on asphaltene deposition mechanisms during CO_2 flooding processes in porous media: a novel experimental study and a modified model based on multilayer theory for asphaltene adsorption. *Energy & Fuels*, **26**, 5080–91.

Juanes R, Spiteri E, Orr F Jr, Blunt M (2006) Impact of relative permeability hysteresis on geological CO_2 storage. *Water Resource Research*, **42**, W12418.

Kim S (2012) CO_2 geological storage: hydro-chemo-mechanically coupled phenomena and engineered injection. In: Civil and Environmental Engineering Atlanta, Georgia Institute of Technology, Ph.D., 188.

Kneafsey TJ, Pruess K (2010) Laboratory flow experiments for visualizing carbon dioxide-induced, density-driven brine convection. *Transport in Porous Media*, **82**, 123–39.

Kopp A, Class H, Helmig R (2009) Investigations on CO_2 storage capacity in saline aquifers: part 1. Dimensional analysis of flow processes and reservoir characteristics. *International Journal of Greenhouse Gas Control*, **3**, 263–76.

Lasaga AC (1984) Chemical kinetics of water-rock interactions. *Journal of Geophysical Research*, **89**, 4009–25.

Li L, Peters CA, Celia MA (2006) Upscaling geochemical reaction rates using pore-scale network modeling. *Advances in Water Resources*, **29**, 1351–70.

Li L, Steefel CI, Yang L (2008) Scale dependence of mineral dissolution rates within single pores and fractures. *Geochimica et Cosmochimica Acta*, **72**, 360–77.

Li H, Wilhelmsen Ø, Lv Y, Wang W, Yan J (2011) Viscosities, thermal conductivities and diffusion coefficients of CO_2 mixtures: review of experimental data and theoretical models. *International Journal of Greenhouse Gas Control*, **5**, 1119–39.

Mangane PO, Gouze P, Luquot L (2013) Permeability impairment of a limestone reservoir triggered by heterogeneous dissolution and particles migration during CO_2-rich injection. *Geophysical Research Letters*, **40**, 4614–19.

Molins S, Trebotich D, Steefel CI, Shen C (2012) An investigation of the effect of pore scale flow on average geochemical reaction rates using direct numerical simulation. *Water Resources Research*, **48**, W03527.

Nordbotten JM, Celia MA, Bachu S (2005) Injection and storage of CO_2 in deep saline aquifers: analytical solution for CO_2 plume evolution during injection. *Transport in porous media*, **58**, 339–60.

Okwen RT, Stewart MT, Cunningham JA (2010) Analytical solution for estimating storage efficiency of geologic sequestration of CO_2. *International Journal of Greenhouse Gas Control*, **4**, 102–7.

Ovaysi S, Piri M (2013) Pore-scale dissolution of CO_2 + SO_2 in deep saline aquifers. *International Journal of Greenhouse Gas Control*, **15**, 119–33.

Ovaysi S, Piri M (2014) Pore-space alteration induced by brine acidification in subsurface geologic formations. *Water Resources Research*, **50**, 440–52.

Patel RA, Perko J, Jacques D, De Schutter G, Van Breugel K, Ye G (2014) A versatile pore-scale multicomponent reactive transport approach based on lattice Boltzmann method: application to portlandite dissolution. *Physics and Chemistry of the Earth, Parts A/B/C*, **70**, 127–37.

Plummer LN, Wigley TML, Parkhurst DL (1978) The kinetics of calcite dissolution in CO_2-water systems at 5–60°C and 0.0 to 1.0 atm CO_2. *American Journal of Science*, **278**, 179–216.

Raoof A, Nick H, Wolterbeek T, Spiers C (2012) Pore-scale modeling of reactive transport in wellbore cement under CO_2 storage conditions. *International Journal of Greenhouse Gas Control*, **11**, S67–77.

Renard F, Gundersen E, Hellmann R, Collombet M, Le Guen Y (2005) Numerical modeling of the effect of carbon dioxide sequestration on the rate of pressure solution creep in limestone: preliminary results. *Oil & Gas Science and Technology*, **60**, 381–99.

Riaz A, Hesse M, Tchelepi HA, Orr FM (2006) Onset of convection in a gravitationally unstable diffusive boundary layer in porous media. *Journal of Fluid Mechanics*, **548**, 87–111.
Saadatpoor E, Bryant SL, Sepehrnoori K (2009) Effect of capillary heterogeneity on buoyant plumes: a new local trapping mechanism. *Energy Procedia*, **1**, 3299–306.
Saripalli P, McGrail P (2002) Semi-analytical approaches to modeling deep well injection of CO_2 for geological sequestration. *Energy Conversion and Management*, **43**, 185–98.
Shin H, Santamarina JC (2009) Mineral dissolution and the evolution of k_0. *Journal of Geotechnical and Geoenvironmental Engineering*, **135**, 1141–7.
Shin H, Santamarina JC, Cartwright JA (2008) Contraction-driven shear failure in compacting uncemented sediments. *Geology*, **36**, 931–4.
Smith MM, Sholokhova Y, Hao Y, Carroll SA (2012) Evaporite caprock integrity: an experimental study of reactive mineralogy and pore-scale heterogeneity during brine-CO_2 exposure. *Environmental Science & Technology*, **47**, 262–8.
Solomon S, Carpenter M, Flach TA (2008) Intermediate storage of carbon dioxide in geological formations: a technical perspective. *International Journal of Greenhouse Gas Control*, **2**, 502–10.
Sposito G (1994) *Chemical Equilibria and Kinetics in Soils*. Oxford University Press, New York.
Steefel CI, Molins S, Trebotich D (2013) Pore scale processes associated with subsurface CO_2 injection and sequestration. *Reviews in Mineralogy and Geochemistry*, **77**, 259–303.
Stumm W, Morgan JJ, Drever JI (1996) *Aquatic Chemistry*. John Wiley and Sons, New York.
Szymczak P, Ladd AJC (2009) Wormhole formation in dissolving fractures. *Journal of Geophysical Research*, **114**, B06203.
Wang X, Gu Y (2011) Oil recovery and permeability reduction of a tight sandstone reservoir in immiscible and miscible CO_2 flooding processes. *Industrial & Engineering Chemistry Research*, **50**, 2388–99.
Weir GJ, White SP, Kissling WM (1996) Reservoir storage and containment of greenhouse gases. *Transport in Porous Media*, **23**, 37–60.
Wigand M, Carey JW, Schütt H, Spangenberg E, Erzinger J (2008) Geochemical effects of CO_2 sequestration in sandstones under simulated *in situ* conditions of deep saline aquifers. *Applied Geochemistry*, **23**, 2735–45.
Zhang Y (2008) *Geochemical Kinetics*. Princeton Univ Press, Princeton.

APPENDIX A

KINETICS—CO_2 DISSOLUTION IN WATER

Injected carbon dioxide CO_2 dissolves in the formation water or brine to sequentially form aqueous carbon dioxide $CO_{2(aq)}$ and carbonic acid H_2CO_3, which consequently dissociates into bicarbonate ions HCO_3^- and hydrogen ions H^+ (Stumm *et al.* 1996; IPCC 2005):

$$CO_{2(g)} \underset{k_{aq}}{\overset{k_g}{\leftrightarrow}} CO_{2(aq)} \qquad K_H = \frac{k_g}{k_{aq}} \tag{A.1}$$

$$CO_{2(aq)} + H_2O \underset{k_{H_2CO_3}}{\overset{k_{CO_2}}{\leftrightarrow}} H_2CO_3 \qquad K = \frac{k_{H_2CO_3}}{k_{CO_2}} \tag{A.2}$$

$$H_2CO_3 \underset{k_{21}}{\overset{k_{12}(\text{very fast})}{\leftrightarrow}} HCO_3^- + H^+ \qquad K_{H_2CO_3} = \frac{k_{12}}{k_{21}} \tag{A.3}$$

The equilibrium constant K [−] for each chemical reaction defines the ratio of produced to reactant species concentrations at equilibrium and can be expressed as a ratio of forward to backward kinetic rates. All rate constants estimated at T~40°C are summarized in Table 1; details follow.

Equation A.1. The rate constant for the dissolution of gaseous carbon dioxide is $k_g \approx 5{\cdot}10^{-3}$ sec^{-1} at T~25°C (Sposito 1994). The rate constant for the reversed direction can be obtained from $k_{aq} = k_g/K_H$, where K_H is Henry's constant.

Equation A.2. The reaction rate constant for hydration is $k_{CO2} \approx 0.04$ sec^{-1} at 25°C with activation energy $E_a = 15$ kcal mol^{-1} and for dehydration is $k_{H_2CO_3} \approx 20$ sec^{-1} at 25°C with $E_a = 16$ kcal mol^{-1} (Stumm *et al.* 1996). The rate constant at a given temperature can be computed using Arrhenius law:

$$k(T) = k_{25} \exp\left[-\frac{E_a}{R}\left(\frac{1}{T} - \frac{1}{298.15}\right)\right] \tag{A.4}$$

where k_{25} is the rate constant at $T = 25$°C(= 298.15 K) and R is the gas constant. Rate constants k_{CO2} and $k_{H_2CO_3}$ are also used to calculate the equilibrium constant K in Eq. A.2.

Equation A.3. Carbonic acid dissociation is very fast compared to reactions in Eqs A.1 and A.2; we selected $k_{12} \approx 10^7$ sec^{-1} at T~40°C (Zhang 2008). The rate constant for the reversed reaction is obtained from $k_{21} = k_{12}/k_{H_2CO_3}$, where the equilibrium constant $Kk_{H_2CO_3}$ is computed from K (Stumm *et al.* 1996):

$$K_{H_2CO_3} = K_1(1 + K) \tag{A.5}$$

where K_1 denotes the first acidity constant for the reaction in which H_2CO_3* dissociates to bicarbonate and hydrogen ions (the asterisk denotes the combination of both aqueous carbon dioxide and carbonic acid). The value of the acidity constant is $K_1 \approx 10^{-6.35}$ under standard conditions.

GEOFLUIDS

Volume 16, Number 2, May 2016
ISSN 1468-8115

CONTENTS

WILEY
Blackwell

Geofluids* is abstracted/indexed in *Chemical Abstracts

This journal is available online at Wiley Online Library.
Visit onlinelibrary.wiley.com to search the articles and register for table of contents and e-mail alerts.